The structures of iron silicate glasses with varying iron redox ratios from molecular dynamics simulations and EXAFS analysis

Manzila I. Tuheen[1], Malin C. Dixon Wilkins[2], John McCloy[2], Jincheng Du[1,*]
[1]Department of Materials Science and Engineering, University of North Texas, Denton, TX
[2]School of Mechanical and Materials Engineering, Washington State University, Pullman, WA

(*Corresponding author. Email: jincheng.du@unt.edu)

Abstract

Iron oxides are frequently found in natural and industrial glass compositions and affect various physical and chemical properties. Thus, a fundamental understanding of iron-bearing silicate melts and glasses is of both scientific and technological importance. This study investigates the structures of sodium iron silicate glasses with compositions of $NaFeSiO_4$, $NaFeSi_2O_6$, $NaFeSi_3O_8$, and $Na_5FeSi_4O_{12}$ using molecular dynamics simulations. Short and medium range structural features of these glasses support that ferrous (Fe^{2+}) and ferric (Fe^{3+}) ions play the roles of network modifier and network former, respectively, with the Fe oxidation states playing an important role in the polymerization of the glass network. These simulation results agree well with newly measured room temperature Extended X-ray Absorption Fine Structure (EXAFS) spectra. The simulated glass structures were compared to simulated melts. The average coordination numbers of the cations are affected both by the melt temperature and iron redox ratio. The coordination environments of the glass formers are affected more by the melt temperature rather than iron redox, whereas for the glass modifier, this trend is not definitive.

Keywords: sodium iron silicate glass, iron redox ratio, molecular dynamics, glass structure, EXAFS, melt structure

Introduction

From their usage in optical devices to applications in the disposal of nuclear waste, silicate glasses have earned their fair share of interest among glass researchers. The inclusion of redox active elements can be used to adjust the physical, chemical, and functional properties of these glasses [1]. Iron is one of the most abundant transition metal elements in igneous rocks and earth materials, with iron-bearing silicate glasses of great importance in geology and Earth science. In addition to this, complex high-level nuclear waste (HLW) melted with glass-forming chemicals and poured in steel containers, such as at the Hanford site, typically contains over 20 elements, with iron oxide (as Fe_2O_3) concentrations ranging from 5 to 30 wt.% [2]. In high iron content HLW, the sodium concentration also varies from 10 to 20 wt.% [3]. A significant body of work is available on the crystallization of iron-containing sodium silicates in HLW and geological systems [4]–[7]. However, further study of iron-containing silicate glasses and melts is still of great significance, with important gaps in the scientific literature yet to be examined.

Generally, iron is added into commercial oxide glass melts in small amounts, either purposefully or as process impurities [8]. Iron can occur in different oxidation states, notably as ferrous (Fe^{2+}) and ferric (Fe^{3+}) ions. Here, the fraction of Fe^{3+} is called the redox ratio (i.e., Fe^{3+}/Fe_{total}), and this equilibrium can be altered by variations in the relative abundance of oxygen in the system. Accordingly, the ferrous-ferric equilibrium can be expressed as a function of temperature, pressure, glass composition, and oxygen fugacity [9]–[13]. At a given oxygen fugacity, with increasing temperature, Fe^{3+} reduces to Fe^{2+} [14], [15]. Also, redox ratio can be secondarily altered by the relative amount of specific alkali present or the basicity of the glass [16]. Mössbauer spectroscopy, wet chemical methods, optical and X-ray spectroscopy, and Raman spectroscopy have all been effectively used to determine the redox ratio in glasses [17]–[21]. Studies by Goldman [22] derived a linear dependence of log (Fe^{2+}/Fe^{3+}) with log(pO_2) and 1/T, where the redox equilibrium does not depend on total iron content in a small range of Fe_2O_3 contents from 0.09 to 0.5 wt.%. Accordingly, this study derived the oxidation-reduction reaction that can be expressed as:

$$Fe^{2+} + (1/4)\ O_2 + (3/2)\ O^{2-} = [Fe^{3+}O_2]^- \quad (1)$$

Presence of various local atomic structural units can tailor the physical properties of iron-bearing silicates. For example: in binary iron silicates, the fraction of ($Fe^{3+}O_4$) tetrahedra controls the

melt viscosity whereas the presence of ($Fe^{2+}O_6$) and ($Fe^{3+}O_6$) octahedra controls the electrical conductivity [23]. Thus, many properties of the final glass, including optical and magnetic properties, crystalline nucleation, viscosity, coloring, and heat capacity, depend largely on the redox ratio of the iron-bearing silicate melts [17], [24]. Establishing relationships between iron-containing silicate melt and glass structures with their bulk properties is essential for numerous geochemical applications. Further to this, a better understanding the role of iron and its redox equilibria will be useful when building and improving prior thermodynamic models [18].

The study of iron-containing glasses is complicated due to disorder effects, along with the presence of two different valence states of iron ions and their interplay. Although significant research has already been performed, there are still relevant debates regarding the roles of these two types of iron ions within glass structures. Some past research suggests that Fe^{3+} works as a network former in the structure, taking up four-fold coordination, *i.e.* a tetrahedral coordination environment [17], [25], [26]. As a consequence, the Fe^{3+} ion polymerizes the glass network and, similar to Al^{3+}, needs to be charge compensated by alkali ions such as Na^+ to ensure overall charge neutrality. In contrast to these findings, there are other studies proving the presence of three- [27], [28] or five- and six-coordinated Fe^{3+} [28], [29]. It is difficult to synthesize glasses containing Fe^{3+} only, limiting the likelihood of quantifying Fe^{3+} sites with coordination states present in minor concentrations [27]. Fe^{2+} has previously been shown to act as a glass network modifier, lowering the melt viscosity and glass transition temperature, T_g, by depolymerizing the glass network. These Fe^{2+} ions generally occupy octahedral sites (six-fold coordination) [18], [26], [30], but there is evidence of five-fold average coordination of ferrous ions occurring as part of a distribution from four to six coordination [28], [31], [32].

Among the wide range of alkaline igneous rocks, equilibrium crystalline and liquid phases in Na_2O-Al_2O_3-Fe_2O_3-SiO_2 system was extensively studied by Bailey and Schairer [33] because of its great petrological importance. Later, Ahmadzadeh *et al.*[34], [35] studied the structure and properties of $NaFeSiO_4$ (Fe-nepheline), $NaFeSi_2O_6$ (acmite), $NaFeSi_3O_8$ (Fe-albite), and $Na_5FeSi_4O_{12}$ (in this work designated as NFS, NFS2, NFS3, and NFS518 respectively) using Raman and Mössbauer spectroscopy. In their study, these glasses were synthesized from Na_2CO_3, Fe_2O_3, and SiO_2 as raw materials. Here, due to the low Si/Fe ratio, Fe-nepheline formed crystalline phase even when undergone a very fast cooling rate whereas acmite and Fe-albite

could readily form amorphous structures. One of the major findings from this study was that most of the iron occurs in four-fold coordinated Fe^{3+}, and when it crystallizes upon isothermal heat treatment as sodium iron silicates, it takes up the octahedral coordination. Understanding of the behavior of these simplified compositions is very important for predicting what phases may crystalline during the production of Fe-rich nuclear waste.

As a result of changes in the iron redox ratio from the melt to the glass during the cooling process, the glass structure also changes during cooling. Considering the potential structural differences in melt and final glass, Nienhuis *et al.* [36] captured the structure of iron-bearing silicate melts using synchrotron X-ray total scattering of liquids suspended by aerodynamic levitation method and furthered the study of Ahmadzadeh *et al.*[34], [35]. Compositions characterized were $NaFeSiO_4$ (*i.e.*, iron-substituted nepheline, iron-substituted carnegieite), $NaFeSi_2O_6$ (*i.e.*, aegirine, acmite, iron-substituted jadeite), $NaFeSi_3O_8$ (*i.e.*, iron-substituted albite). Melts were produced in a container-less aerodynamic levitation process paired with laser heating. Fitting of the obtained X-ray scattering data was used to extract a melt structure by empirical potential structure refinement (EPSR) and compared to structures obtained from classical molecular dynamics (MD) simulations.

To build upon the understanding of sodium iron silicate melts studied by levitation and in-situ high energy X-ray diffraction coupled with RMC and MD simulations [36], the current work focuses on the investigation of the final glass structure of these glass compositions using classical MD simulations. Additional challenges faced in the studies of iron-containing amorphous materials is that nuclear magnetic resonance (NMR) spectroscopy normally used for structural studies is adversely affected due to the paramagnetic nature of iron [37]. Therefore, MD simulations have special potential in the investigation of glass systems containing iron. Alongside glass compositions studied by Nienhuis *et al.*[36], the other sodium-iron-silicate $Na_5FeSi_4O_{12}$ (NFS518) is also included in the current study of glass structure. Finally, the Fe K-edge Extended X-ray Absorption Fine Structure (EXAFS) spectra of glasses with compositions matching NFS, NFS2, NFS3 and NFS518, alongside crystallized samples of NFS2 and NFS518, have also been collected, and analyzed for this study for the first time, to act as an experimental comparison.

Detailed MD simulations with well-tested partial charge pairwise potentials were used to generate structural models of the glass systems using experimentally measured room-temperature redox ratios of the glasses. For comparison, glasses with the predicted melt redox ratio were also simulated and compared with those with previously measured glass redox ratios. Short and medium range structural features were characterized by calculating the pair distribution functions, bond angle distributions, ring size distribution, and Q_n distributions.

The paper is organized as follows: the simulation methodologies and EXAFS experiments are reported followed by the results. Discussions based on the findings in this work with others in the literature are then presented and followed by a conclusion.

Methodologies

Experimental methods

The glasses and glass-ceramics examined here were produced as described in Ahmadzadeh *et al*. [34, 35]. Briefly, stoichiometric amounts of oxides and carbonates were heated in air to 1500 °C for 1 hour, before being quenched on removal from the furnace. Crystallized versions of NFS2 and NFS518 were obtained by heat treating the resulting glass for 24 h at 900°C or 700°C, respectively.

Fe K-edge X-ray absorption spectra were collected at NSLS-II beamline 6BM (Brookhaven National Laboratory, USA). The beamline was configured with a Rh-coated paraboloid collimating mirror, a Si (111) monochromator, and a flat harmonic rejection mirror. Samples were prepared by pressing sufficient material to form one absorption length into pellets with (poly)ethylene glycol as a low absorbing inert binder. Measurements were conducted at room temperature in transmission mode. Signal intensity of the incident and transmitted X-rays were measured using ionization chambers operating in a stable range of their current *vs.* voltage curve. The spectra of the pristine and crystallized glasses were collected alongside reference compounds of known Fe oxidation state and average coordination number (CN) (aegirine, Fe^{3+}, 6 CN; $FePO_4$, Fe^{3+}, 4 CN; $FeCO_3$, Fe^{2+}, 6 CN; staurolite, Fe^{2+}, 4 CN). Data were analyzed in Athena and Artemis, parts of the Demeter software suite [38]. Some details of these measurements have been previously reported, including the X-ray absorption near-edge structure (XANES) and analysis of the pre-edge for NFS, NFS2, NFS3, and crystallized NFS3 [34].

Simulation details

Table 1 Glass compositions, densities and redox ratios used in the study[34], [35]

Glass ID	Mineral analogue name	Chemical Formula	Glass redox % Fe^{3+} [34], [35]	SiO_2	Fe_2O_3	FeO	Na_2O	Density Exp. (g/cm^3)	Cell Size (Å)	Density MD (g/cm^3)
				%mole						
NFS	Fe-nepheline	$NaFeSiO_4$	100	50.00	25.00	0	25.00	3.004	48.400	2.975
NFS2	Acmite	$NaFeSi_2O_6$	88	65.36	14.38	3.92	16.34	2.781	48.788	2.792
NFS3	Fe-albite	$NaFeSi_3O_8$	91	74.17	11.25	2.22	12.36	2.612	49.277	2.658
NFS518	-	$Na_5FeSi_4O_{12}$	93	56.86	6.61	0.99	35.54	2.685	55.119	2.681

Classical molecular dynamics simulations were used to generate the structures of glasses with compositions listed in Table 1. The interactions among the atoms are described by the Born model of solids combined with partial-charge pairwise potentials. These partial-charge pairwise potentials consist of short-range Buckingham and long-range coulombic interaction terms and can be expressed in the form presented in Eq. 2.

$$V(r_{ij}) = \frac{Z_i Z_j e^2}{4\pi\varepsilon_o r_{ij}} + A_{ij}\exp(-r_{ij}/\rho_{ij}) - C_{ij}/r_{ij}^6 \quad (2)$$

Where r_{ij} stands for the interatomic distance between two ions i and j; e and ε_0 are the electric charge and the permittivity of vacuum, respectively; A, ρ, and C are the different parameters for the Buckingham term. To better describe the partial covalent and ionic nature of the chemical bonds present in these systems, partial but constant charges of the ions are adopted in the columbic part of the potential (Z_i and Z_j for ions i and j respectively). In Table 2, the Buckingham term related parameters and the partial charges of the ions are tabulated. The empirical potential set used in this work was that developed by Teter and revised by Deng and Du [39], [40]. A correction term is included in this potential set to predict correct trajectories and melt structures at high temperature [41]. This empirical potential has been successfully used in

diverse multi-component glass systems and efficiently derived the structures and properties [42]–[48]. Nienhuis et al. [36] successfully used this potential set to predict the melt structure of the same set of glass compositions in Table 2.

Molecular dynamics simulations were performed to generate the structures of the glass composition from Table 1 using the DL_POLY 2.20 software package developed by Smith and Forester at Daresbury Laboratory, UK [49]. For short range interactions, the cutoff distance was taken to be 8 Å. For long-range interactions, the Ewald summation method, with relative precision of 1×10^{-6} and a cutoff distance of 10 Å, was used. A Verlet Leapfrog algorithm with a time step of 1 fs was used to integrate the equations of motion. The initial glass structures were generated by putting atoms randomly in a cubic box called the simulation cell. In this work, each simulation cell contained approximately 8000 atoms. More information on the simulation cell can be found in Table S1. The dimensions of each initial box were such that it replicates the room temperature densities from experiments of the corresponding glass compositions [34, 35]. These initially generated glass structures were then subjected to a simulated melt-quench process [50]. In this process, each randomly generated initial glass structure was energy minimized at 0 K and relaxed at 300 K followed by a heating up to 6000 K under canonical ensemble conditions (constant number, volume, and temperature, NVT) to obtain a uniform, fully liquid melt. The molten glass was then cooled down with a nominal cooling rate of 1 K/ps under the NVT ensemble. At the final temperature (300 K) and pressure (1 atm), for every 50 configurations of the last 60,000 steps, the trajectory was recorded. This structure is the MD simulated final structure of the glass, used for analysis of the short- and medium-range structure of the glasses. Structural information, such as the pair distribution functions (PDF), coordination number (CN), bond angle distribution (BAD), and Q_n distribution, were extracted using the methods described by Deng and Du [51]. The cutoff distances used in this process for different pairs were determined from the value of the first minimum in the respective plots of partial total correlation functions.

As we performed fixed charge classical MD simulations, we could not dynamically adjust iron oxidation states, and hence the redox ratios were fixed and did not evolve with temperature. Instead, glasses with different iron redox ratios were simulated by using the fraction of ferric and ferrous iron based on measured or theoretically predicted redox ratios. Then corresponding

amount of Fe^{3+} and Fe^{2+} ions were introduced in the initial configuration and the redox remained the same during the melt and quench process. This approach has been used in previous simulation work to address the iron redox ratios in borosilicate [52] and phosphate glasses [53], [54].

Table 2 Atomic charges and Buckingham potential parameters

Pairs	A_{ij} (eV)	ρ_{ij} (Å)	C_{ij} (eV·Å^6)	B_{ij} (eV·Å^6)	D_{ij}	n
$O^{-1.2}$-$O^{-1.2}$	2029.2204	0.343645	192.58	46.462	-0.32605	3.430
$Si^{2.4}$-$O^{-1.2}$	13702.905	0.193817	54.681	28.942	-3.0250	3.949
$Na^{0.6}$-$O^{-1.2}$	4383.7555	0.243838	30.70	48.251	-4.7037	2.898
$Fe^{1.2}$-$O^{-1.2}$	11777.0703	0.207132	21.642	104.203	-32.110	2.670
$Fe^{1.8}$-$O^{-1.2}$	19952.29	0.182538	4.6583	260.9828	-340.739	2.115

Results

Neutron and X-ray diffraction

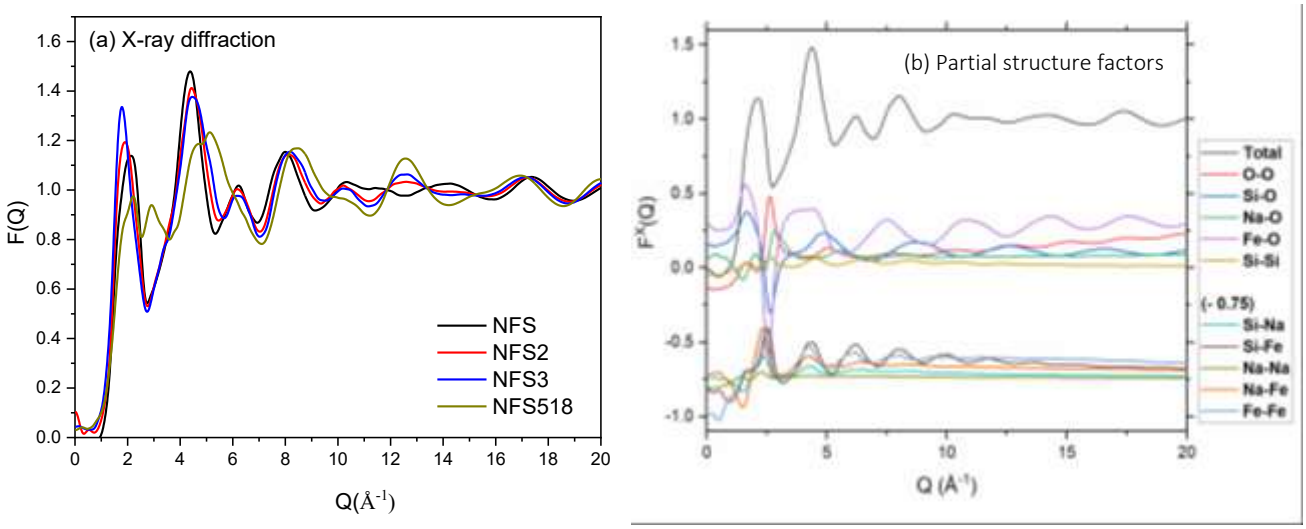

Figure 1 Calculated (a) X-ray diffraction total structure factor for NFS, NFS2, NFS3 and NFS518, and (b) X-ray partial structure factor for NFS (cation-cation partial structure factors (except Si-Si) are offset by -0.75 for clarity.

Total X-ray diffraction structure factors of the MD simulated NFS, NFS2, NFS3 and NFS518 glasses are shown in Figure 1 (a). These structure factors are derived from the partial distribution functions obtained from MD simulated structure through Fourier transformations using Lorch type window functions. It can be seen that the first sharp diffraction peak (FSDP) that provides information regarding the medium range order decreases in intensity with increasing amount of iron oxide and sodium oxide. This is consistent with other silicate glasses that showed a decrease trend of FSDP intensity with increasing modifier content. The partial structure factors for NFS are shown in Figure 1 (b), which shows that the contribution to FSDP (located at ~2.10 $Å^{-1}$) is mainly from the Si-O and Fe-O pairs. The second peak or the primary peak (located at ~4.36 $Å^{-1}$), on the other hand, is mainly from contributions from Fe-O and cation-cation pairs such as Si-Fe, Fe-Fe, Fe-Na and Si-Na. Neutron structure factors of all the glasses were also calculated (see Fig. S1) and showed similar behavior of FSDP with composition.

Bond distance and coordination environment

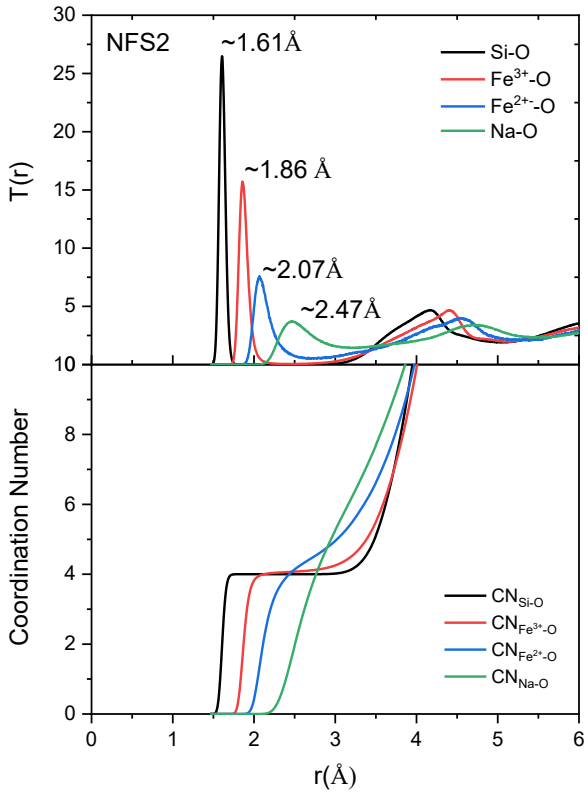

Figure 2 Partial total correlation functions and cation coordination numbers in simulated NFS2 glass

Table 3 Cation-oxygen bond distances in simulated NFS2 glass composition

Cation-oxygen pairs	Bond Length, Å	Experiment	*ab initio*
Si-O	1.61	1.60-1.61 [55]	1.64 [56]
Fe^{3+}-O	1.86	1.94 [57]	1.86 [58]
Fe^{2+}-O	2.07	2.12 [57]	2.00 [58]
Na-O	2.47	2.30-2.43 [55], 2.46-2.62 [59]	2.36-2.43 [56]

Figure 2 shows the partial total correlation functions, T(r), of different cation-oxygen pairs and cation coordination numbers in the simulated NFS2 glass structure, representative of the simulated glass compositions. The peaks observed in T(r) indicate the bond distance of that corresponding cation-oxygen pair. The bond distances obtained for Si-O, Fe^{3+}-O, Fe^{2+}-O, and Na-O are reported and compared with experimental and *ab initio* studies in Table 3. In this study, the Si-O bond length is around 1.60 Å, which is a close match with previous findings for silicate glasses, based on X-ray diffraction techniques [55]. The two types of iron cation, ferrous (Fe^{2+}) and ferric (Fe^{3+}), have significantly different curves in the T(r) plot. Fe^{3+}-O shows a sharper and narrower first coordination peak, similar to the Si-O pair, whereas Fe^{2+}-O creates a broader peak more similar to that of the Na-O pair. Divalent Fe^{2+} also has a significantly longer Fe-O bond length than trivalent Fe^{3+} (2.07 Å and 1.86 Å, respectively), with the corresponding values both in good agreement with those identified by high energy X-ray diffraction of iron-containing phosphate glasses [57]. In the current EXAFS study, the Fe-O bond was 1.87 Å for all compositions except NFS518 which was 1.89 Å, indicating the majority of Fe is Fe^{3+}. The Na-O bond distance obtained in this study is approximately 2.47Å, which is in the range previously determined in reports utilized X-ray absorption spectroscopies (*i.e.*, EXAFS and XANES) to study silica-rich sodium aluminosilicate systems [55], [59].

From the plot of oxygen coordination (Figure 2), it can be observed that Fe^{3+} has an increase in coordination number, followed by a plateau at a coordination of 4 and then a further increase. This is similar to the behavior of glass formers (such as Si) in these systems. On the other hand, the coordination number of Fe^{2+} varies more significantly, and closely resembles that of Na, a network modifier. These are in agreement with the findings from previous experiments [5], [18], [30] and MD simulations [13], [52] where trivalent iron was shown to behave as a glass network former and divalent iron as a glass network modifier. The cation-oxygen coordination distributions and average coordination numbers of the glass formers and modifiers are listed in Tables 4-5. As expected, the average coordination number of Si is 4 in all cases, regardless of the glass composition (Table S2). The average coordination number of Fe^{3+} is approximately 4 in all compositions, but there is a small contribution from higher coordination numbers (mostly five-coordination) in all compositions. The maximum fraction of five-fold coordinated Fe^{3+} was observed in the NFS518 glass structure, at approximately 13.35%. The average coordination of Fe^{2+} in NFS glass series is around 4.5, with a significant fraction of five-fold coordinated Fe

(from 27.59% to 31.68% of the total Fe^{2+}) as well as a smaller contribution from six-fold coordinated Fe (from 2.50% to 8.62% of the total Fe^{2+}). Na^{+} has an average coordination of approximately 6.3, with six- and seven-fold coordination having the largest contributions. Na^{+} ion coordination showed the widest range of coordination environments, with the majority of Na^{+} ions falling into four-fold to nine-fold coordination (Table S3).

Table 4 Coordination number distribution (%) and mean coordination of Fe^{3+}

	3	4	5	6	Avg Coord.
NFS	0.06	92.12	7.70	0.12	4.08
NFS2	0.03	93.27	6.65	0.05	4.06
NFS3	0.74	94.47	4.77	0.02	4.05
NFS518	0.00	86.49	13.35	0.16	4.13

Table 5 Coordination number distribution (%) and mean coordination of Fe^{2+}

	3	4	5	6	Avg Coord
NFS	N/A	N/A	N/A	N/A	N/A
NFS2	2.97	58.42	31.68	6.93	4.43
NFS3	12.07	51.72	27.59	8.62	4.33
NFS518	2.50	65.00	30.00	2.50	4.33

Cation-Cation Partial distribution function (PDF)

A pair distribution function (PDF) is a 1D function that describes the structural correlations within a material [60]. By definition, in an amorphous material with M number of component, M(M+1)/2 PDFs provide a complete description of the system [61]. The cation-oxygen PDFs provide important information on the coordination of each cation by oxygen while the cation-cation PDFs provide information on the correlation of cation-oxygen polyhedrons. Figure 3 shows the partial PDFs of the cation-cation pairs in the simulated glass structures. Some of the

PDFs are noisier than others due to the lower number of species (*e.g.* the Fe^{2+}-Fe^{2+} PDF). Since PDFs are calculated by normalizing to the number of atoms of both species involved, the peak intensities provide information of the probability of occurrence of a particular linkage [62]. For example, in Figure S2, from the overlapping curves of cation-cation PDFs, it can be concluded that these glasses are mostly made of Si-Si correlations (*i.e.*, Si-O-Si linkages), then there are a significant number of Si-O-Fe^{3+} linkages and least number of Fe^{3+}-O-Fe^{3+} linkages, suggesting that Fe^{3+} enters the Si-O glass network while the [FeO_4] tetrahedra do not usually link to each other which can be understood by the negative charge associated with the units. Comparing the cation-cation PDFs of Si and/or Fe^{3+} with either Fe^{2+} or Na reveals that there is not a particular preference for these network modifiers to be linked to any particular glass forming species. An interesting feature can be extracted from Figure S2 where the NFS2, NFS3, and NFS518 glass compositions have significant intensity for Fe^{2+}-Fe^{2+} correlations (*i.e.*, Fe^{2+}-O- Fe^{2+} linkages). This could be due to the tendency for ferrous iron to cluster in these sodium iron silicate glasses. To be able to relate these phenomena to the redox ratio of the glasses, a significant number of glass compositions with varying redox ratios would need to be studied.

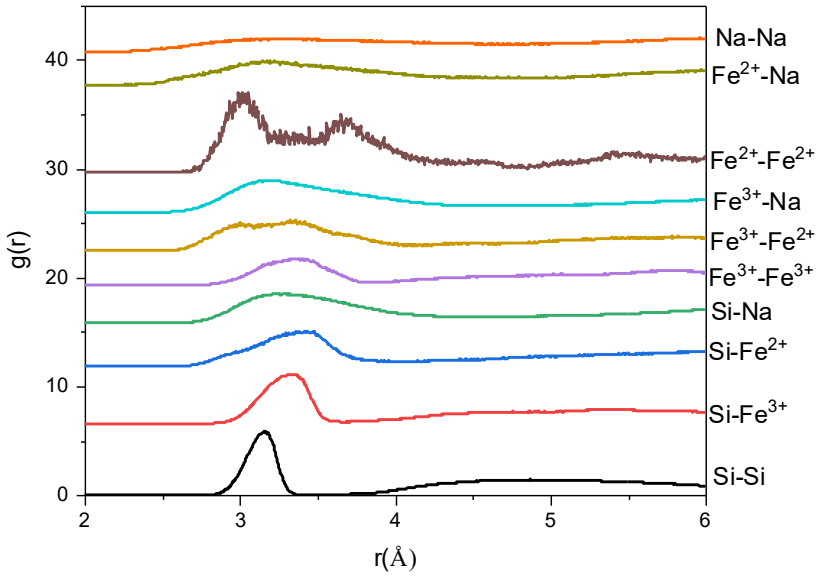

Figure 3 Partial Pair distribution functions of the cation-cation pairs in simulated NFS2 glass compositions

Bond angle distributions

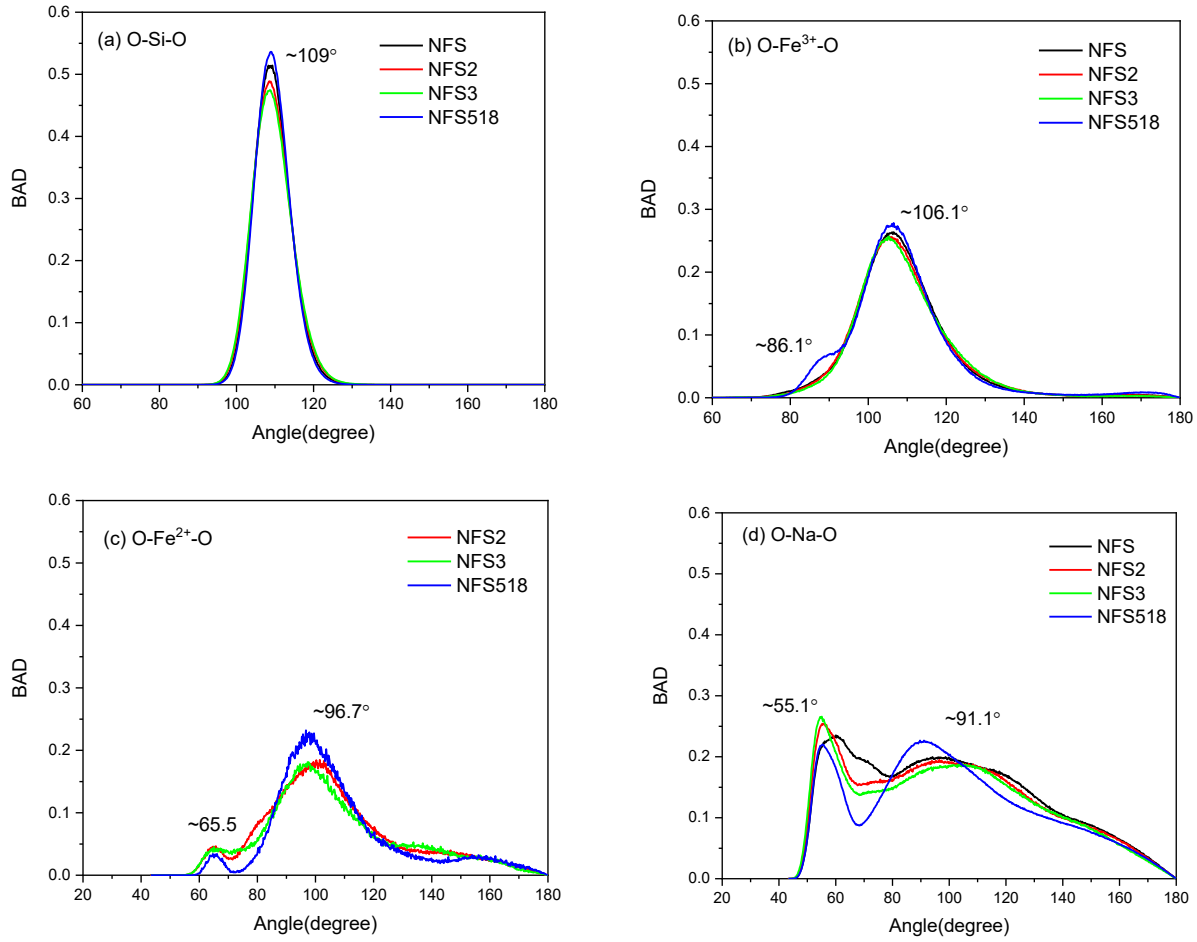

Figure 4 O-Cation-O bond angle distributions of the glass formers with surrounding oxygen: (a) O-Si-O, (b) O-Fe^{3+}-O, (c) O-Fe^{2+}-O, and (d) O-Na-O

Figure 4 shows the O-X-O bond angle distributions (BAD) for the cations(X) in the glass, which can be used to gain an understanding of the consistency of the glass forming tetrahedron. Here, O-Si-O had a bond angle distribution maximum at approximately 108.9°, very close to the 109.47° bond angle of an ideal tetrahedron (Figure 4a). This finding is in accordance with previous X-ray diffraction and neutron scattering studies of amorphous and vitreous silica [63], [64]. Similar to Si, the BAD of O-Fe^{3+}-O has a maximum at approximately 106.1° (Figure 4b), which results from tetrahedral coordination of Fe^{3+}, though with a broader distribution than Si

due to significant populations of under- and over-coordinated ferric ions. This value is similar to the obtained value in previous MD simulations of iron-containing boro-alumino-silicate glasses [52]. It was observed that, in case of NFS518 glass composition, the O-Fe^{3+}-O BAD has an additional feature at approximately 86.1° which results from the trigonal bipyramidal shape of the more significant fraction of five-coordinated Fe^{3+} present in this composition, see Table 4. BAD of the modifiers Fe^{2+} and Na are shown Figure 4c and 4d, respectively. The O-Fe^{2+}-O BAD shows an extended distribution from approximately 50° to 180° with two prominent maxima around 64.7° and 98.3°, depending on the composition. Similarly, the O-Na-O BAD extends from approximately 45° to 180° with two distinguishable maxima at approximately 54.5° and 101.3°. As explained by Xiang and Du [65], the higher angle features (*e.g.* the maxima at approximately 101.3°) in the BAD of network modifiers relate to the coordination of the modifier by non-bridging oxygens from two separate glass-forming polyhedron, in this case [SiO_4] and [FeO_4] tetrahedrons. On the other hand, the features at lower angles (*e.g.* the maxima at approximately 54.5°) of the network modifier BAD result from coordination by two oxygen ions from the same glass forming polyhedron. The positions of higher angle features in O-Fe^{2+}-O BAD are observed to be shifted toward slightly lower angle (from approximately 100° to 97.3°) with increasing redox ratio (Fe^{3+}/Fe_{tot}). The shape of the BAD of O-Na-O is significantly altered as a result of introducing Fe^{2+} ions in the glass compositions from NFS to NFS2 and NFS3 and even more so for NFS518 which has a significantly higher Na/Fe ratio.

Figure S3 shows the X-O-X BADs of the simulated glass structures which represent the connectivity of the network forming tetrahedron. For Si-O-Si, Si-O-Fe^{3+} and Fe^{3+}-O-Fe^{3+}, BAD peaks remain at ~150°, 140°, and 120°, respectively, and though differences in overall glass composition caused changes in the relative intensities of these peaks, the peak positions are not significantly altered. Given the NFS glass has the least amount of silicon, the prevalent polyhedral linkage is Si-O-Fe^{3+}. But with as the relative fraction of silicon increases (from NFS2 to NFS518), Si-O-Si becomes the preferred polyhedral linkage. In all except NFS, the relative abundance of Fe^{3+}-O-Fe^{3+} linkages are the lowest among the X-O-X connections, demonstrating that it is the least preferred polyhedral linkage in these glass systems. This reluctance to form

Fe^{3+}-O-Fe^{3+} linkage is similar to Lowenstein's alumina avoidance which is observed in aluminum-containing glasses both by experiment [66], [67] and MD simulations [52].

Oxygen speciation

Table 6 lists the oxygen speciation in the three glass compositions. The lowest fraction of non-bridging oxygens (NBO) is seen in the NFS glass, where all the iron is present as Fe^{3+}, and NBO are generated due to the presence of sodium only. The NFS3 glass, with an increased fraction of ferrous ions, has a slightly increased fraction of NBO compared to NFS. The glass with the highest fraction of iron as Fe^{2+}, the NFS2 glass, shows the highest amount of NBOs, which is a further indication of the network modifying behavior of ferrous iron in these systems. These results are consistent with the assignment of Fe^{2+} ions as network modifiers in this study, as well as previously reported experiments and MD simulations [52], [68].

A significantly increased fraction of NBO in the NFS518 glass was observed, which is best explained by difference in the relative fractions of Na and Fe in these compositions (Table 1). For the glasses NFS to NFS3, the Na concentration is equal to (NFS) or only slightly higher (NFS2, NFS3) than the abundance of Fe^{3+}. This means that the majority of Na ions are able to charge compensate Fe^{3+} tetrahedron, with little left to generate NBO in NFS, NFS2, and NFS3 glasses. In comparison, the NFS518 composition contains a significantly higher ratio of Na to Fe, meaning a relatively high fraction of Na is available to generate NBO.

Table 6 Oxygen coordination environments (% distribution) in Na-Fe-Si glass systems

	Non-bridging (1)	Bridging (2)	Tri-bridging (3)	Free Oxygen (0)
NFS	4.85	88.35	6.80	-
NFS2	7.80	89.39	2.78	0.02
NFS3	5.16	92.56	2.25	-
NFS518	34.24	65.64	0.09	0.03

Q^n distribution of the glass formers

The distributions of Q_n species are important when examining the medium range structure and degree of polymerization of a glass system. Here, Q_n identifies glass forming units with *n* bridging oxygens (from Q_0 to Q_4) linked to it. Table 7-8 summarize the Q_n distributions of [SiO_4]

and [FeO_4] polyhedrons in the NFS glass series. It can be observed that silicon is mostly observed as Q_4 species (four bridging oxygens to each of the tetrahedron) species in all glass compositions except NFS518 (Table 7). Among the NFS, NFS2, and NFS3 glass compositions, NFS2 has the lowest fraction of Q_4 species, most likely since it contains the highest fraction of Fe^{2+}. In the NFS518 glass composition, due to the presence of a significantly larger Na:Fe ratio, the silicate glass network is noticeably depolymerized, giving rise to higher fractions of Q_1, Q_2, and Q_3 species. As seen for the Si tetrahedron, Fe^{3+} glass forming units are predominantly Q_4, but with significant fractions of Q_3 and Q_5 species present as well (Table 8). Like in the silicate network, Q_4 species of Fe^{3+} are notably reduced in the NFS518 composition, with a corresponding increase in Q_3 and Q_5 species, as well as a small fraction of Q_2 species. The presence of significant Fe^{3+} Q_4 species in all compositions is further evidence that it behaves as a glass network former, with Q_4 units polymerizing the glass network in three dimensions.

Table 7 Q_n distributions of silicon (Si) glass networks in % of total Si

	Q_1	Q_2	Q_3	Q_4
NFS	0.00	0.98	15.14	83.88
NFS2	0.12	1.42	18.43	80.03
NFS3	0.00	0.41	12.30	87.29
NFS518	3.65	21.62	45.44	29.29

Table 8 Q_n distributions of ferric (Fe^{3+}) glass networks in % of total Fe^{3+}

	Q_2	Q_3	Q_4	Q_5	Q_6
NFS	0.00(1)	2.27	90.00	7.61	0.12
NFS2	0.00(1)	3.20	90.44	6.31	0.05
NFS3	0.00(3)	2.60	92.61	4.77	0.02
NFS518	0.95	8.57	77.40	12.92	0.16

Ring size distribution

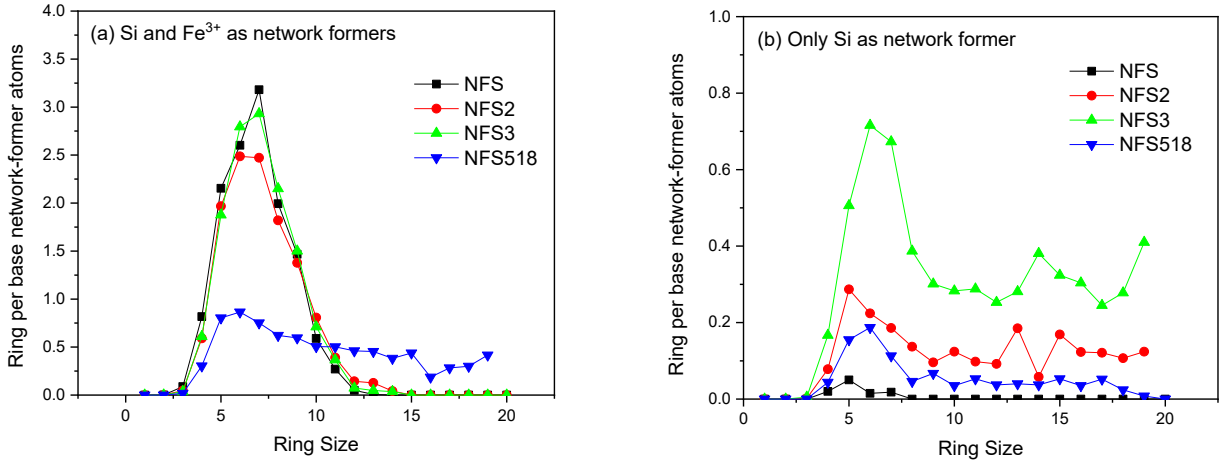

Figure 5 Ring-size distribution of the simulated glass compositions considering (a) both Si and Fe^{3+} and (b) only Si as glass network formers

Ring size distribution is another important medium-range structural feature of a glass network, showing the relative fractions of rings made up of different numbers of corner-sharing network forming polyhedron. When a ring contains the minimum number of polyhedrons, it is called a primitive ring [44]. In the case of pure vitreous silica, ring size is a symmetric Gaussian distribution with the center at approximately six [39]. With the incorporation of glass modifiers, the glassy silicate network depolymerizes and larger membered rings become more common [69]. Figure 5a shows the primitive ring size distributions of the simulated glass compositions, considering both Si and Fe^{3+} as glass network formers. For NFS, NFS2 and NFS3, they show very similar ring size distributions with ring size centered around 5-7 membered rings. These three glasses are charge balanced with, Fe^{3+}/Na^{+} ratios of approximately 1:1 (neglecting the small fractions of Fe^{2+} present in some compositions). Similarity of ring size distribution of the three glasses suggests that Fe^{3+} enters the glass forming network and plays similar roles as Si in forming the ring structures. For NFS518, it has a higher free network modifier content (*i.e.* Na that is not necessary to charge balance Fe^{3+} tetrahedrons) hence the glass network structure is more depolymerized, with higher fractions of larger rings. For comparison, Figure 5b shows ring size distribution considering only Si as glass former. In this case, for NFS3 with SiO_2 comprising 75% of the network forming cations, the peak position is around six, whereas for the NFS2 and NFS1 glass, the intensity of the main peak drops significantly since only part of the rings in the

glass forming network were considered. For NSF518, there are no significant ring structures due to high modifier fractions. This further supports that Fe^{3+} enters the glass network structures and plays an important role linking the fragments of Si-O networks.

Comparisons between melt and glass structure

Nienhuis *et al.* [36] analyzed the structures of NFS, NFS2 and NFS3 melts *via* synchrotron X-ray total scattering also modeled the melt structures using EPSR and MD simulations. Comparisons between melt and glass structures are one of the major aspects of the current study. Redox ratios of the melt structures were predicted by the redox model of Jayasuriya *et al.* [70], which were taken as the melt redox ratios for MD simulations[36]. Composition of the melt along with the redox ratio is presented in Table 9. Melt structures at 3500 K were modelled and analyzed. The redox ratios obtained from ^{57}Fe Mössbauer spectra and wet chemical methods reported by Ahmadzadeh *et al.* [34] were used for the MD simulations of room temperature glass structures which is reported in Table 1. An additional set of simulations was also performed to generate glass structures with melt redox ratios in order to distinguish between the effect of redox and temperature. Two models of each glass structure at 300 K, those with glass redox and those with melt redox, were also analyzed.

Figure 6 shows the partial total correlation functions of the melt and glass structures of the simulated NFS series. For the network forming species (Si^{4+} and Fe^{3+}), the peaks are broadened with lower intensities than glass structures indicating significant temperature-induced broadening of the first coordination shell. Similar broadening was also observed for the network modifiers Fe^{2+} and Na. There are no visible shifts in peak position in the partial distribution functions for melt and glass structures. The partial total correlation functions of the glasses with glass redox ratios and glasses with melt redox ratios coincide closely with each other.

Table 9 Melt composition and redox ratio of NFS glass series (3500K)

Glass ID	Melt redox % Fe^{3+} [36]	SiO_2	Fe_2O_3	FeO	Na_2O
		%mole			
NFS	29	42.46	6.16	30.15	21.23
NFS2	19	58.73	2.79	23.79	14.69
NFS3	15	67.80	1.69	19.21	11.30

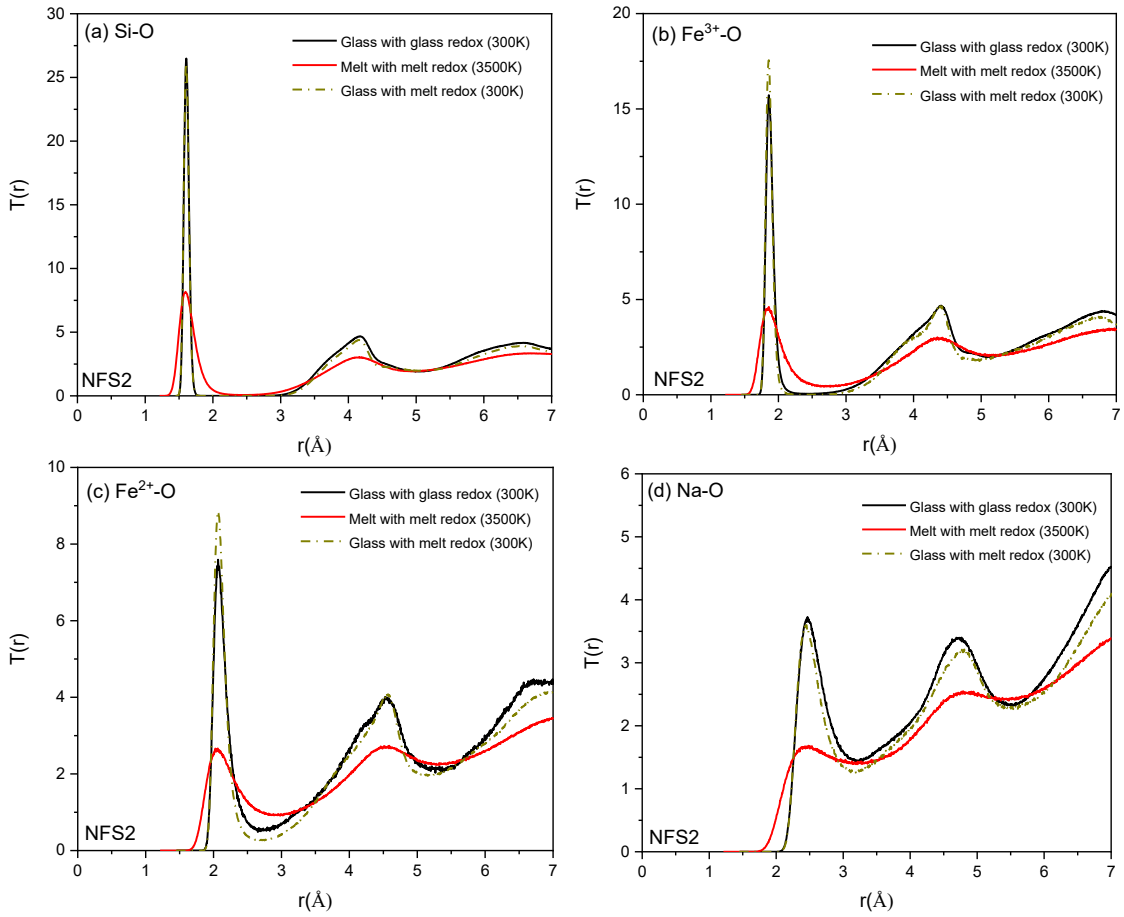

Figure 6 Partial total correlation functions of (a) Si-O, (b) Fe^{3+}-O, (c) Fe^{2+}-O, and (d) Na-O in simulated NFS2 melt and glasses with different Fe redox ratios

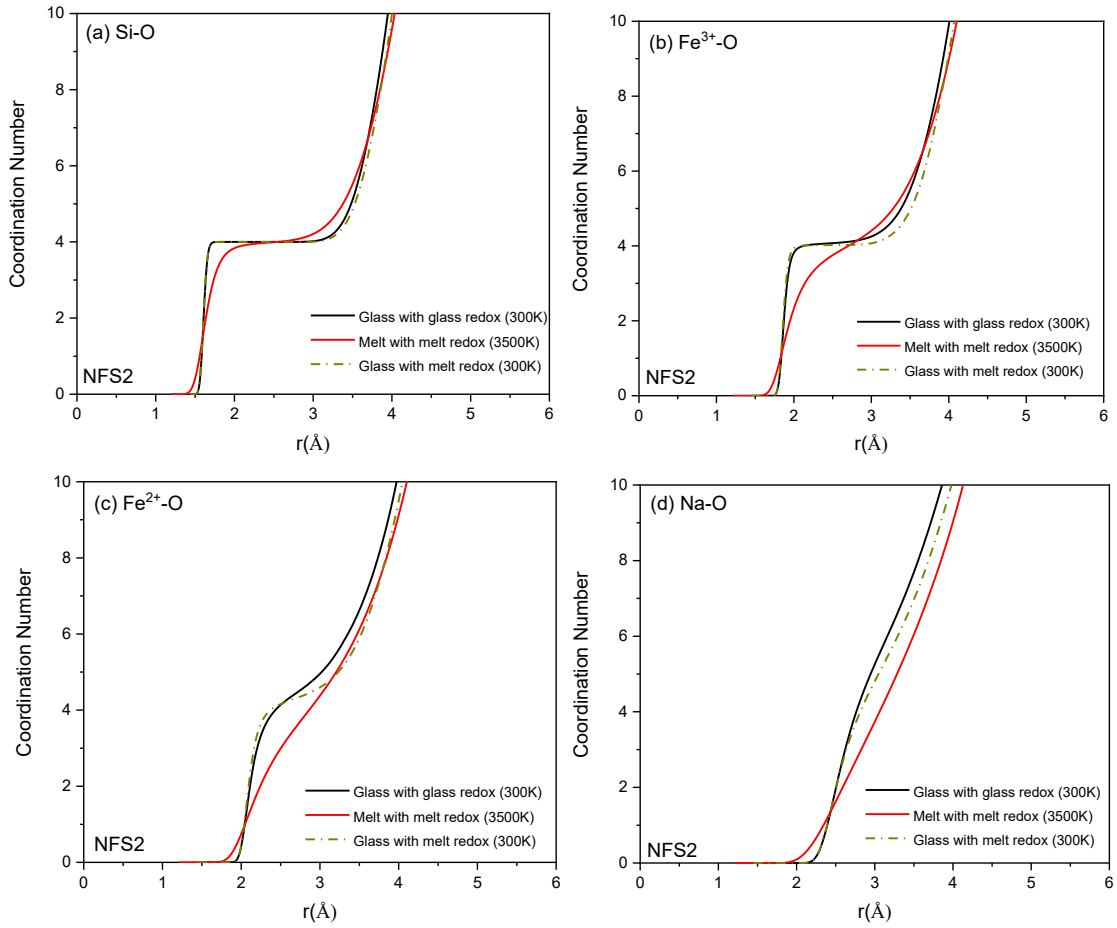

Figure 7 Distribution of oxygen coordination number around (a) Si, (b) Fe^{3+}, (c) Fe^{2+}, and (d) Na in simulated NFS2 glass and melt with different redox ratios

Figure 7 shows the cumulative oxygen coordination around the cations in the NFS2 melt and glass structures from MD simulations. The average coordination numbers are summarized in Table S4. Both Si^{4+} and Fe^{3+} have slightly lower average coordination in the melt compared to in the glass structures. However, the network formers have almost identical coordination environments in the two glass structures, that with the glass redox ratio and that with the melt redox ratio. Therefore, it can be concluded that, rather than redox ratio, temperature has a much greater influence on the average oxygen coordination number of the network formers. With respect to the network modifier cations Fe^{2+} and Na^{+}, both temperature and redox ratio have strong effects on their coordination numbers.

Fe K-edge X-ray absorption spectroscopy

The analysis of the pre-edge features observed in the Fe K-edge spectra of the NFS1, NFS2 and NFS3 glasses and crystallized NFS2 has been previously reported by Ahmadzadeh *et al.* [34], so will only be briefly discussed here, alongside the equivalent analyses of the spectra of a NFS518 glass and crystallized NFS518, which has not yet been reported.

In agreement with the simulations detailed above, Fe is, within the detection limit of Fe K-edge XANES, predominantly present in all glasses as tetrahedrally coordinated Fe^{3+} (i.e. $^{[4]}Fe^{3+}$), with pre-edge features of reasonable intensity centered at approximately 7113.3 eV. When comparing the features observed for each glass, some variation in pre-edge integrated intensity is seen, with NFS1 and NFS2 having the most intense features and NFS518 the least intense. Given the dependence of Fe K-edge pre-edge features on the centrosymmetry of the Fe environment (generally octahedrally coordinated Fe leads to low integrated intensities and tetrahedrally coordinated Fe leads to high integrated intensities, with 5 coordinate Fe approximately between), this is in good agreement with the mean coordination numbers derived from the simulations detailed above (see **Error! Reference source not found.**), and the previously reported Mössbauer spectroscopy of NFS1, NFS2, NFS3 and crystallized NFS2 [34]. In contrast to the glassy materials, the crystallized NFS2 and NFS518 materials appeared, within the detection limit of Fe K-edge XANES, to contain only Fe^{3+} in predominantly octahedral environments, in good agreement with the previously reported crystal structures of aegirine [71] and $Na_5FeSi_4O_{12}$ [35].

Fitting of the extended X-ray absorption fine structure (EXAFS) was also performed, to further confirm the Fe coordination environments in these materials, see Table 10. In all cases, reasonable fits were found where the first shell coordination of Fe matched those expected from previous reports, the simulations detailed above, and the observed spectral pre-edge features. Preliminary fits examining different Fe coordination environments were performed, with the coordination environments from the best fits carried forward to the final fitting procedures. The glasses NFS1, NFS2, NFS3 and NFS518 contained Fe predominantly in 4-coordinate environments (i.e., Fe^{3+}-O distance of 1.87 – 1.89 Å), and the crystallized NFS2 and NFS518 glasses contained Fe predominantly in 6-coordinate environments (i.e., Fe^{3+}-O distance of 1.91 – 2.07 Å). Bond valence sums were calculated from the coordination numbers and bond lengths

derived from EXAFS fitting and corresponded to approximately Fe^{3+} in all cases. These results are in good agreement with the Fe coordination environments seen in the simulated glass structures where, though small fractions (approximately 10% of the total Fe content in NFS2, NFS3 and NFS518) of higher-coordinated Fe^{2+} were present in some compositions, 4-coordinate Fe^{3+} predominated in all glasses. Plots of these EXAFS fits as performed in the Artemis platform [72] can be found in the Supplementary Information (Figures S4 – S11).

Table 10: Details of fits of Fe K-edge EXAFS spectra shown in Supplementary Figures S4 – S11. Degeneracies (coordination number) of the Fe-O_1 scattering path were set to either 4 (tetrahedral Fe), 6 (octahedral Fe), or 4+2 (distorted octahedral Fe), with only the degeneracy corresponding to the best fit reported. Degeneracy of Fe-Fe and Fe-Na were set to 2 and Fe-Si set to 6 in all cases.

	NFS1	**NFS2**	**NFS3**	**NFS518**	**NFS2 Crys.**	**NFS518 Crys.**
E_0 (eV)	0.58±0.34	0.52±0.62	0.05±0.55	1.02±1.46	0.08±1.03	-1.39±1.22
R_{Fe-O1} (Å)	1.87(1)	1.87(1)	1.87(1)	1.89(1)	1.91(1) 2.07(1)	2.00(1)
N_{Fe-O1}	4	4	4	4	4 2	6
R_{Fe-O2} (Å)	3.21(5)	3.21(11)	3.22(8)	3.68(10)	-	-
σ^2_O (Å^2)	0.005(3)	0.005(1)	0.004(1)	0.004(1)	0.007(2)	0.005(1)
R_{Fe-Fe} (Å)	2.81(5)	3.26(35)	3.30(4)	3.21(10)	3.20(3)	-
σ^2_{Fe} (Å^2)	0.025(9)	0.001(4)	0.010(4)	0.005(16)	0.010(4)	-
R_{Fe-Si} (Å)	3.25(2)	3.25(3)	3.24(3)	3.25(6)	3.24(3)	3.30(5)
σ^2_{Si} (Å^2)	0.020(2)	0.002(4)	0.026(15)	0.013(13)	0.018(4)	0.001(3)
R_{Fe-Na} (Å)	2.91(3)	3.11(4)	2.91(8)	3.28(13)	-	3.23(6)
σ^2_{Na} (Å^2)	0.011(5)	0.0003(4)	0.015(10)	0.001(21)	-	0.017(12)
R factor	*0.003*	*0.008*	*0.005*	*0.015*	*0.005*	*0.012*
Fe BVS (v.u.)	*2.75(16)*	*2.77(19)*	*2.77(19)*	*2.62(21)*	*3.29(30)*	*2.90(17)*
Red. chi-sq	1300.29	6005.01	1640.68	1600.43	4108.87	93.33

NOTES: E_0 is the fitted absorption edge position; R_{X-Y} is the bond length between X and Y atoms, N_{Fe-O1} is the coordination number of nearest neighbor oxygen atoms (O1) around Fe; σ^2_X is the Debye-Waller factor for X; R factor is a measure of the goodness-of-fit; Fe BVS is the bond valence sum in valence units; Red. chi-sq is the reduced χ^2 of the fit. The amplitude reduction factor S_0^2 for all fits was 0.6356, obtained by fitting a crystalline aegirine mineralogical standard. FEFF scattering paths were chosen from crystallographic information files for aegirine (*i.e.*, crystalline NFS2), in most cases, but NFS518 crystals in the case of the 518 glass and crystallized glass.

Discussions

Molecular dynamics (MD) simulation is a potent way to explore the structures and properties of amorphous and glassy materials. This method can provide insight into important structural aspects which are difficult or impossible to obtain by experimental methods. The choice of appropriate empirical potentials is also vital for deriving accurate data from MD simulations. In this work, we focused on the structural analysis of iron-bearing sodium silicate glasses as a continuation of the previously performed in-situ melt analysis of the same glass compositions [36]. We applied MD with Deng and Du's [40] potentials, with additional iron-related parameters, and this proved to be effective for multicomponent iron-bearing glasses and melts [36], [52]. Using this potential set, structures of $NaFeSiO_4$, $NaFeSi_2O_6$, $NaFeSi_3O_8$ and $Na_5FeSi_4O_{12}$ (glass ID: NFS, NFS2, and NFS3, and NFS518, respectively) were simulated. These glasses have particular importance in the management of certain high-Fe nuclear wastes as well as in geo-scientific studies. Essential structural features were examined for these glass compositions along with comparisons between the melt and glassy structures.

Comparison of MD and EXAFS results

Though the results from the MD were not used as inputs to the EXAFS analysis, it is useful to compare typical Fe environments and coordination numbers from MD versus those used for fitting the EXAFS. In the case of the MD simulations, the cut-off distance for determining the coordination number was found by the minimum in the pair distribution function (PDF). It was previously shown that even when doing experimental PDF, there is not perfect agreement with MD bond lengths and coordination [36]. In the EXAFS fits, the coordination numbers were not left as free parameters. Multiple fits were performed, using 4-coordinate (tetrahedral), 4+2-coordinate (distorted octahedral) and 6-coordinate (octahedral) environments; the path degeneracies were then fixed to the best fit for the final fits shown in Table 11. In doing this, the bond distance is refined in all cases, though this does not correspond exactly to the cut-off values for the MD.

For the Fe-O coordination, the MD shows a value very close to 4.0, which is what was used for the EXAFS. For the Fe-Fe coordination, the MD predicts a sensible reduction of this coordination, going from a high value of 2.43 for the highest Fe composition (NFS) to a low value of 0.53 for the most dilute Fe composition (NFS518). By contrast, the EXAFS spectra arenot particularly sensitive to this, with Fe being the third nearest neighbor (or even the fourth

nearest neighbor for those compositions having more second nearest neighbor oxygen (see Table 10). Similarly, the Fe-Si coordinations vary in the MD with Fe/Si ratio, as one would expect, but the EXAFS fits are relatively insensitive to this, and a fixed value of 6 was an improvement in the overall fit for all compositions. Finally, the Fe-Na coordinations according to MD are highest for NSF518 (composition with the most Na), then next highest for the two highest Fe samples (NFS and NFS2) and lowest for the highest Si sample (NFS3). EXAFS, again, was insensitive to these differences. The EXAFS fits were reasonable with only nearest neighbor oxygens, but improved slightly with the addition of second nearest neighbors, as listed below in Table 11 and shown in the Supplementary Information. This indicates that, as is well known, most EXAFS data, especially for multi-component amorphous materials, is relatively indeterminate for second nearest neighbors. This shows the value of using MD, potentially even as an input for initial models experimental local structure fitting.

Table 11. Cut-off distances and computed coordination numbers from MD as compared to degeneracies (CN) and bond lengths from EXAFS

MD Cutoff (Å)	2.5 **Fe-O**	3.88 **Fe-Fe**	4.6 **Fe-Na**	3.67 **Fe-Si**
EXAFS bond length (Å)	1.79-1.89	2.81 (NFS) 3.21-3.30 (other glasses)	2.91-3.18 (significant variations)	3.24- 3.25
Assumed EXAFS CN	4	2	2	6
MD Determined CN:				
NFS	4.09	2.43	4.75	2.4
NFS2	4.07	1.27	3.49	3.46
NFS3	4.04	1.03	2.8	3.27
NFS518	4.14	0.53	6.55	3.6

General discussion on the structure of natural materials

The simulated bond distances of the cation-oxygen pairs are in good agreement with the EXAFS derived Fe-O bond lengths discussed here, as well as previous experimental and *ab initio* studies. As expected in these systems, the bond distance of Fe^{3+}-O is observed to be significantly shorter than Fe^{2+}-O. In the structures of the three types of mineral-like analogues, Fe-nepheline, aegirine, Fe-albite (note that only aegirine is a true mineral [34]) silicon is four-fold coordinated by oxygen in all cases. Therefore, only [SiO_4] tetrahedra take part in forming the glass network.

On substitution of Fe_2O_3 for SiO_2, ferric iron is being incorporated and also forms part of the glass network. This is also evident from the bond angle distributions in Figure S3, where the feature intensities of Si-O-Fe^{3+} increased significantly as the relative silica content was increased from NFS to NFS3. It should also be noted that Fe^{3+}-O-Fe^{3+} were the least preferred linkages, a phenomenon which should be compared to the rule of [AlO_4] avoidance [73]. The ring size distribution considering both Si and Fe^{3+} in Figure 5a show similar distributions for NFS, NFS2 and NFS3, supporting the observation that Fe^{3+} actively takes part in the otherwise Si-O dominated glass network. Ferric iron in these systems is predominantly four-fold coordinated, although there are significant populations of higher and lower coordination numbers. In these systems, ferrous iron also has a maximum coordination number at four but with a significantly broader distribution, *i.e*. higher fractions of 3-, 5-, and 6-fold coordinated iron. Sodium was approximately 6.3 coordinated by oxygen in all compositions, varying in the range from 6.49 to 6.11 from NFS to NFS518.

The differing roles of Fe^{2+} and Fe^{3+}

The system examined here contains two valence state of iron: ferrous and ferric. These iron ions have different roles in the structures of these glasses. It appears that ferrous iron behaves as a glass modifier and the ferric iron behaves as a glass former. As shown in Table 4, we observed that the average coordination number of Fe^{3+} is approximately 4 in all glasses, varying from 4.05 to 4.13. On the other hand, see Table 5, ferrous ions have broader distributions of first shell coordination, with an average coordination close to 4.5 (from 4.33 to 4.43). Also, in the plot of coordination as described by the partial total correlation function (Figure 2), it can be observed that ferric iron was coordinated similarly to Si, *i.e.* similar to that of a glass network former, with a more significant plateau in coordination number. In contrast, ferrous iron displayed a trend in coordination more similar to the network modifier Na, with a more gradual change in slope and no significant plateau. The role of Fe^{2+} as a network modifier role was again observed in the trends in O speciation, see Table 6. Here, among NFS, NFS2, and NFS3 glass compositions (assuming all Na is charge compensating Fe^{3+} polyhedra and not generating NBO), NFS2 with the highest fraction of Fe^{2+} shows the highest abundance of non-bridging oxygen. This is also observed when considering the polymerization of the Si network as a function of composition, again with the Si network in NFS2 (having the highest fraction of ferrous iron) being less polymerized than those in NFS and NFS3, see Table 7. In contrast, the presence of Fe^{2+} does not

seem to have a significant effect on the speciation of Fe^{3+} polyhedrons in these glass systems, see Table 8. Considering the trends previously observed for cations with higher cationic field strength [74], it can be concluded that Fe^{2+} is more effective in creating NBO than aiding in polyhedral charge compensation in these glass systems.

Comparison between melt and glass structures

Analysis of the structural features of both melt and cooled glass are equally important, with significant variations observed in many systems. In this work we studied the glass structures and compared them to the melt structures previously reported, taking into consideration both the effect of the Fe redox ratio and the temperature. First, we simulated melt and glass structures for the NFS series at 3500 K and 300 K with redox ratios corresponding to the melt and the final glass. In addition, the glass structure at 300 K was also simulated with a redox ratio corresponding to the melt, in order to isolate the effect of temperature on the glass structures from the effect of the redox ratio. We conclude that there is no significant change in average oxygen coordination number of the network formers due to iron redox, though these values varied significantly with temperature, particularly due to temperature induced broadening of the bond distance distributions. On the other hand, the average coordination number of the network modifiers changed with both temperature and iron redox ratio. This can be explained by the lower cation field strength of these modifier cations, with their coordination more easily influenced by the change of temperature and redox chemistry.

Conclusions

In this study, the structures of $NaFeSiO_4$, $NaFeSi_2O_6$, $NaFeSi_3O_8$, and $Na_5FeSi_4O_{12}$ glass compositions were investigated using MD simulations with partial charge pairwise potentials. Short- and medium range structural information was thoroughly analyzed in the glass phases. The results compare well with the short-range structures observed by fitting of experimental Fe K-edge EXAFS spectra. One of the important objectives of this study was to observe the effect of the Fe redox ratio, with iron present in two different valence states: ferric and ferrous. Ferric iron takes part in network formation whereas ferrous iron performs the role of a glass modifier, similar to a typical divalent alkaline earth. Ferrous ions exhibited a tendency to cluster, which should be further studied to establish their effects on the crystallizing behavior of these glasses. Overall, this study adds to our understanding of Fe-containing glass structures, with significant

implications for the design of glass materials containing Fe, as well as when examining the structures of magmatic silicate liquids.

Acknowledgements

JD acknowledges support from National Science Foundation (project #1662288). Glass synthesis and experimental studies were funded by the Department of Energy, Office of Environmental Management, through the Office of River Protection, Waste Treatment and Immobilization Plant Federal Project Office, contract number 89304017CEM000001, under the direction of Dr. Albert A. Kruger. A portion of this research used 6-BM of the National Synchrotron Light Source II (NSLSII), a U.S. DOE OS user facility operated for the DOE OS by Brookhaven National Laboratory (BNL) under contract DE-SC0012704.

Description of supplemental information

Atom box parameters; Coordination number distribution of Si and Na; Calculated neutron structure factor; Cation-cation partial pair distribution functions; Average oxygen coordination numbers; XANES spectra, including pre-edge; EXAFS fits; EXAFS fit summary.

References

[1] V. Magnien *et al.*, "Kinetics of iron redox reactions in silicate liquids: A high-temperature X-ray absorption and Raman spectroscopy study," *J. Nucl. Mater.*, vol. 352, no. 1–3, pp. 190–195, 2006, doi: 10.1016/j.jnucmat.2006.02.053.

[2] A. A. Kruger *et al.*, "Final Report Melt Rate Enhancement for High Aluminum HLW Glass Formulations," 2008.

[3] D. S. Kim *et al.*, "Formulation and characterization of waste glasses with varying processing temperature," 2011.

[4] C. M. Jantzen and K. G. Brown, "Predicting the spinel-nepheline liquidus for application to nuclear waste glass processing. Part II: Quasicrystalline freezing point depression model," *J. Am. Ceram. Soc.*, vol. 90, no. 6, pp. 1880–1891, 2007, doi: 10.1111/j.1551-2916.2006.01028.x.

[5] B. Cochain, D. R. Neuville, G. S. Henderson, C. A. McCammon, O. Pinet, and P. Richet, "Effects of the iron content and redox state on the structure of sodium borosilicate glasses: A Raman, Mössbauer and boron k-edge xanes spectroscopy study," *J. Am. Ceram. Soc.*, vol. 95, no. 3, pp. 962–971, 2012, doi: 10.1111/j.1551-2916.2011.05020.x.

[6] J. J. BENTZEN, "Three Crystalline Polymorphs of KFeSiO4, Potassium Ferrisilicate," *J. Am. Ceram. Soc.*, vol. 66, no. 7, pp. 475–479, 1983, doi: 10.1111/j.1151-2916.1983.tb10584.x.

[7] M. Ahmadzadeh, J. Marcial, and J. McCloy, "Crystallization of iron-containing sodium

aluminosilicate glasses in the NaAlSiO4-NaFeSiO4 join," *J. Geophys. Res. Solid Earth*, vol. 122, no. 4, pp. 2504–2524, 2017, doi: 10.1002/2016JB013661.

[8] E. S. Dunaeva *et al.*, "Coordination and RedOx ratio of iron in sodium-silicate glasses," *J. Non. Cryst. Solids*, vol. 358, no. 23, pp. 3089–3095, 2012, doi: 10.1016/j.jnoncrysol.2012.08.004.

[9] J. A. Duffy, "Redox equilibria in glass," *J. Non. Cryst. Solids*, vol. 196, no. 95, pp. 45–50, 1996, doi: 10.1016/0022-3093(95)00560-9.

[10] B. O. Mysen and D. Virgo, "Structure and Properties of Silicate Glasses and Melts; Theories and Experiment BT - Advanced Mineralogy: Volume 1 Composition, Structure, and Properties of Mineral Matter: Concepts, Results, and Problems," A. S. Marfunin, Ed. Berlin, Heidelberg: Springer Berlin Heidelberg, 1994, pp. 238–254.

[11] W. D. JOHNSTON, "Oxidation-Reduction Equilibria in Molten Na2O.2SiO2 Glass," *J. Am. Ceram. Soc.*, vol. 48, no. 4, pp. 184–190, 1965, doi: 10.1111/j.1151-2916.1965.tb14709.x.

[12] R. K. Kukkadapu *et al.*, "Mössbauer and optical spectroscopic study of temperature and redox effects on iron local environments in a Fe-doped (0.5 mol% Fe2O3) 18Na2O-72SiO2 glass," *J. Non. Cryst. Solids*, vol. 317, no. 3, pp. 301–318, 2003, doi: 10.1016/S0022-3093(02)01815-X.

[13] C. Weigel, L. Cormier, G. Calas, L. Galoisy, and D. T. Bowron, "Nature and distribution of iron sites in a sodium silicate glass investigated by neutron diffraction and EPSR simulation," *J. Non. Cryst. Solids*, vol. 354, pp. 5378–5385, 2008, doi: 10.1016/j.jnoncrysol.2008.09.030.

[14] C. Le Losq, M. R. Cicconi, and D. R. Neuville, "Iron in silicate glasses and melts: implications for volcanological processes," *ESSOAr*, pp. 1–29, 2020.

[15] B. O. Mysen and P. Richet, "Silicate Glasses and Melts: Properties and Structure," *Elsevier Sci.*, 2005.

[16] M. R. Cicconi, G. Giuli, W. Ertel-Ingrisch, E. Paris, and D. B. Dingwell, "The effect of the [Na/(Na+K)] ratio on Fe speciation in phonolitic glasses," *Am. Mineral.*, vol. 100, no. 7, pp. 1610–1619, 2015, doi: 10.2138/am-2015-5155.

[17] P. A. Bingham, J. M. Parker, T. Searle, J. M. Williams, and K. Fyles, "Redox and clustering of iron in silicate glasses," *J. Non. Cryst. Solids*, vol. 253, no. 1–3, pp. 203–209, 1999, doi: 10.1016/S0022-3093(99)00361-0.

[18] Z. Wang, T. F. Cooney, and S. K. Sharma, "In situ structural investigation of iron-containing silicate liquids and glasses," *Geochim. Cosmochim. Acta*, vol. 59, no. 8, pp. 1571–1577, 1995, doi: 10.1016/0016-7037(95)00063-6.

[19] B. O. Mysen, F. Seifert, and D. Virgo, "Structure and redox equilibria of iron-bearing silicate melts," *Am. Mineral.*, vol. 65, no. 9–10, pp. 867–884, 1980.

[20] M. Bonnin-Mosbah, A. S. Simionovici, N. Métrich, J. P. Duraud, D. Massare, and P. Dillmann, "Iron oxidation states in silicate glass fragments and glass inclusions with a

XANES micro-probe," *J. Non. Cryst. Solids*, vol. 288, no. 1–3, pp. 103–113, 2001, doi: 10.1016/S0022-3093(01)00611-1.

[21] L. Galoisy, G. Calas, and M. A. Arrio, "High-resolution XANES spectra of iron in minerals and glasses: Structural information from the pre-edge region," *Chem. Geol.*, vol. 174, no. 1–3, pp. 307–319, 2001, doi: 10.1016/S0009-2541(00)00322-3.

[22] D. S. GOLDMAN, "Oxidation Equilibrium of Iron in Borosilicate Glass," *J. Am. Ceram. Soc.*, vol. 66, no. 3, pp. 205–209, 1983, doi: 10.1111/j.1151-2916.1983.tb10018.x.

[23] C. Shi, O. L. G. Alderman, A. Tamalonis, R. Weber, J. You, and C. J. Benmore, "Redox-structure dependence of molten iron oxides," *Commun. Mater.*, vol. 1, no. 1, pp. 1–7, 2020, doi: 10.1038/s43246-020-00080-4.

[24] B. O. Mysen, "Redox equilibria of iron and silicate melt structure: Implications for olivine/melt element partitioning," *Geochim. Cosmochim. Acta*, vol. 70, no. 12, pp. 3121–3138, 2006, doi: 10.1016/j.gca.2006.03.014.

[25] G. B. Cook, R. F. Cooper, and T. Wu, "CHEMICAL DIFFUSION AND CRYSTALLINE NUCLEATION DURING OXIDATION OF 1 . Introduction : dynamic oxidation , structure and nucleation in iron-bearing amorphous silicates," *J. Non. Cryst. Solids*, vol. 120, pp. 207–222, 1990.

[26] M. Magini *et al.*, "On the coordination of iron ions in sodium borosilicate glasses," *J. Non. Cryst. Solids*, vol. 65, no. 1, pp. 145–159, 1984, doi: 10.1016/0022-3093(84)90362-4.

[27] C. Weigel, L. Cormier, L. Galoisy, G. Calas, D. Bowron, and B. Beuneu, "Determination of Fe3+ sites in a NaFeSi2O6 glass by neutron diffraction with isotopic substitution coupled with numerical simulation," *Appl. Phys. Lett.*, vol. 89, no. 14, pp. 1–4, 2006, doi: 10.1063/1.2359532.

[28] F. Farges, Y. Lefrère, S. Rossano, A. Berthereau, G. Calas, and G. E. Brown, "The effect of redox state on the local structural environment of iron in silicate glasses: A combined XAFS spectroscopy, molecular dynamics, and bond valence study," *J. Non. Cryst. Solids*, vol. 344, no. 3, pp. 176–188, 2004, doi: 10.1016/j.jnoncrysol.2004.07.050.

[29] Q. Liu and R. A. Lange, "The partial molar volume of Fe2O3 in alkali silicate melts: Evidence for an average Fe3+ coordination number near five," vol. 91, no. 2–3, pp. 385–393, 2006, doi: doi:10.2138/am.2006.1902.

[30] B. O. Mysen, "The structural behavior of ferric and ferrous iron in aluminosilicate glass near meta-aluminosilicate joins," *Geochim. Cosmochim. Acta*, vol. 70, no. 9, pp. 2337–2353, 2006, doi: https://doi.org/10.1016/j.gca.2006.01.026.

[31] S. Rossano, A. Y. Ramos, and J. M. Delaye, "Environment of ferrous iron in CaFeSi2O6 glass; contributions of EXAFS and molecular dynamics," *J. Non. Cryst. Solids*, vol. 273, no. 1–3, pp. 48–52, 2000, doi: 10.1016/S0022-3093(00)00124-1.

[32] W. E. Jackson *et al.*, "Multi-spectroscopic study of Fe(II) in silicate glasses: Implications for the coordination environment of Fe(II) in silicate melts," *Geochim. Cosmochim. Acta*, vol. 69, no. 17, pp. 4315–4332, 2005, doi: 10.1016/j.gca.2005.01.008.

[33] D. K. Bailey and J. F. Schairer, “Crystallization of the rock-forming silicates in the system Na2O-Fe2O3-Al2O3-SiO2 at 1 atmosphere,” *Carnegie Inst. Washingt. Year B.*, vol. 62, pp. 124–131, 1963.

[34] M. Ahmadzadeh *et al.*, “Structure of NaFeSiO4 , NaFeSi2 O6, and NaFeSi3 O8 glasses and glass-ceramics Mostafa,” *Am. Mineral. Vol.*, vol. 105, pp. 1375–1384, 2020.

[35] M. Ahmadzadeh, T. A. Olds, A. Scrimshire, P. A. Bingham, and J. S. McCloy, “Structure and properties of Na5FeSi4O12 crystallized from 5Na2O–Fe2O3–8SiO2 glass,” *Acta Crystallogr. Sect. C Struct. Chem.*, vol. 74, no. 12, pp. 1595–1602, 2018, doi: 10.1107/S2053229618014353.

[36] E. T. Nienhuis, M. Tuheen, J. Du, and J. S. Mccloy, “In situ pair distribution function analysis of crystallizing Fe-silicate melts,” *J. Mater. Sci.*, vol. 56, no. 9, pp. 5637–5657, Mar. 2021, doi: 10.1007/s10853-020-05643-x.

[37] R. Youngman, “NMR spectroscopy in glass science: A review of the elements,” *Materials (Basel).*, vol. 11, no. 4, 2018, doi: 10.3390/ma11040476.

[38] B. Ravel and M. Newville, “{\it ATHENA}, {\it ARTEMIS}, {\it HEPHAESTUS}: data analysis for X-ray absorption spectroscopy using {\it IFEFFIT},” *J. Synchrotron Radiat.*, vol. 12, no. 4, pp. 537–541, Jul. 2005, doi: 10.1107/S0909049505012719.

[39] J. Du and A. N. Cormack, “Molecular dynamics simulation of the structure and hydroxylation of silica glass surfaces,” *J. Am. Ceram. Soc.*, vol. 88, no. 9, pp. 2532–2539, 2005, doi: 10.1111/j.1551-2916.2005.00352.x.

[40] L. Deng and J. Du, “Development of boron oxide potentials for computer simulations of multicomponent oxide glasses,” *J. Am. Ceram. Soc.*, vol. 102, no. 5, pp. 2482–2505, 2019, doi: 10.1111/jace.16082.

[41] J. Du and L. Rene, “Compositional dependence of the first sharp diffraction peaks in alkali silicate glasses : A molecular dynamics study,” vol. 352, pp. 3255–3269, 2006, doi: 10.1016/j.jnoncrysol.2006.05.025.

[42] Y. Xiang, J. Du, M. M. Smedskjaer, and J. C. Mauro, “Structure and properties of sodium aluminosilicate glasses from molecular dynamics simulations,” *J. Chem. Phys.*, vol. 139, no. 4, Jul. 2013, doi: 10.1063/1.4816378.

[43] J. Du and A. N. Cormack, “Erratum: ‘The medium range structure of sodium silicate glasses: A molecular dynamics simulation’ by J. Du and A.N. Cormack (Journal of Non-Crystalline Solids (2004) 349 (66-79) DOI:10.1016/j.jnoncrysol.2004.08.264),” *J. Non. Cryst. Solids*, vol. 351, no. 10–11, 2005, doi: 10.1016/j.jnoncrysol.2005.02.002.

[44] J. Du and A. N. Cormack, “The medium range structure of sodium silicate glasses: A molecular dynamics simulation,” *J. Non. Cryst. Solids*, vol. 349, no. 1–3, pp. 66–79, 2004, doi: 10.1016/j.jnoncrysol.2004.08.264.

[45] M. Ren, L. Deng, and J. Du, “Bulk, surface structures and properties of sodium borosilicate and boroaluminosilicate nuclear waste glasses from molecular dynamics simulations,” *J. Non. Cryst. Solids*, vol. 476, pp. 87–94, Nov. 2017, doi: 10.1016/j.jnoncrysol.2017.09.030.

[46] M. I. Tuheen, L. Deng, and J. Du, "A comparative study of the effectiveness of empirical potentials for molecular dynamics simulations of borosilicate glasses," *J. Non. Cryst. Solids*, vol. 553, no. July 2020, p. 120413, 2021, doi: 10.1016/j.jnoncrysol.2020.120413.

[47] X. Lu, M. Ren, L. Deng, C. J. Benmore, and J. Du, "Structural features of ISG borosilicate nuclear waste glasses revealed from high-energy X-ray diffraction and molecular dynamics simulations," *J. Nucl. Mater.*, vol. 515, pp. 284–293, 2019.

[48] M. I. Tuheen and J. Du, "Structural features and rare earth ion clustering behavior in lanthanum phosphate and aluminophosphate glasses from molecular dynamics simulations," *J. Non. Cryst. Solids*, vol. 578, no. December 2021, p. 121330, 2022, doi: 10.1016/j.jnoncrysol.2021.121330.

[49] I. Todorov, W. Smith, and U. Cheshire, "The DL POLY 4 user manual," *STFC, STFC Daresbury …*, no. January, 2011.

[50] A. Pedone, "Properties Calculations of Silica-Based Glasses by Atomistic Simulations Techniques : A Review," pp. 20773–20784, 2009.

[51] L. Deng and J. Du, "Development of effective empirical potentials for molecular dynamics simulations of the structures and properties of boroaluminosilicate glasses," *J. Non. Cryst. Solids*, vol. 453, pp. 177–194, 2016, doi: 10.1016/j.jnoncrysol.2016.09.021.

[52] M. I. Tuheen, W. Sun, and J. Du, "Effect of iron redox ratio on the structures of boroaluminosilicate glasses," *J. Am. Ceram. Soc.*, vol. 105, no. 12, pp. 7272–7290, Dec. 2022, doi: 10.1111/jace.18685.

[53] K. Joseph *et al.*, "Iron phosphate glasses: Bulk properties and atomic scale structure," *J. Nucl. Mater.*, vol. 494, pp. 342–353, Oct. 2017, doi: 10.1016/j.jnucmat.2017.07.015.

[54] K. Joseph, K. Jolley, and R. Smith, "Iron phosphate glasses: Structure determination and displacement energy thresholds, using a fixed charge potential model," *J. Non. Cryst. Solids*, vol. 411, pp. 137–144, 2015, doi: 10.1016/j.jnoncrysol.2014.12.033.

[55] G. N. Greaves, A. Fontaine, P. Lagarde, D. Raouxt, and S. J. Gorman, "Local structure of silicate glasses," *Nature*, vol. 293, no. October, pp. 611–616, 1981, doi: 10.1038/293611a0.

[56] M. Fortino *et al.*, "Assessment of interatomic parameters for the reproduction of borosilicate glass structures via DFT-GIPAW calculations," *J. Am. Ceram. Soc.*, vol. 102, no. 12, pp. 7225–7243, 2019, doi: 10.1111/jace.16655.

[57] U. Hoppe, M. Karabulut, E. Metwalli, R. K. Brow, and P. Jóvári, "The Fe-O coordination in iron phosphate glasses by x-ray diffraction with high energy photons," *J. Phys. Condens. Matter*, vol. 15, no. 36, pp. 6143–6153, 2003, doi: 10.1088/0953-8984/15/36/305.

[58] P. Stoch, W. Szczerba, W. Bodnar, M. Ciecinska, A. Stoch, and E. Burkel, "Structural properties of iron-phosphate glasses: Spectroscopic studies and ab initio simulations," *Phys. Chem. Chem. Phys.*, vol. 16, no. 37, pp. 19917–19927, 2014, doi: 10.1039/c4cp03113j.

[59] D. A. McKeown, G. A. Waychunas, and G. E. Brown, "Exafs and xanes study of the local coordination environment of sodium in a series of silica-rich glasses and selected minerals within the Na2OAl2O3SiO2 system," *J. Non. Cryst. Solids*, vol. 74, no. 2–3, pp. 325–348, 1985, doi: 10.1016/0022-3093(85)90078-X.

[60] M. W. Terban and S. J. L. Billinge, "Structural Analysis of Molecular Materials Using the Pair Distribution Function," *Chem. Rev.*, vol. 122, no. 1, pp. 1208–1272, 2022, doi: 10.1021/acs.chemrev.1c00237.

[61] J. D. Westwood and P. Georgopoulos, "A Maximum Entropy Method of Determining the Partial Distribution Functions OF Multicomponent Amorphous Materials," *J. Non. Cryst. Solids*, vol. 108, pp. 169–179, 1989.

[62] D. A. Keen, "A comparison of various commonly used correlation functions for describing total scattering," *J. Appl. Crystallogr.*, vol. 34, no. 2, pp. 172–177, 2001, doi: 10.1107/S0021889800019993.

[63] H. F. Poulsen, J. Neuefeind, H. B. Neumann, J. R. Schneider, and M. D. Zeidler, "Amorphous silica studied by high energy X-ray diffraction," *J. Non. Cryst. Solids*, vol. 188, no. 1–2, pp. 63–74, 1995, doi: 10.1016/0022-3093(95)00095-X.

[64] D. I. Grimley, A. C. Wright, and R. N. Sinclair, "Neutron scattering from vitreous silica IV. Time-of-flight diffraction," *J. Non. Cryst. Solids*, vol. 119, no. 1, pp. 49–64, 1990, doi: 10.1016/0022-3093(90)90240-M.

[65] Y. Xiang and J. Du, "Effect of strontium substitution on the structure of 45S5 bioglasses," *Chem. Mater.*, vol. 23, no. 11, pp. 2703–2717, Jun. 2011, doi: 10.1021/cm102889q.

[66] J. Stebbins, "Aluminium avoidance avoided," *Nature*, vol. 330, no. 6143, pp. 13–14, 1987, doi: 10.1038/330013a0.

[67] D. M. Zirl and S. H. Garofalini, "Structure of Sodium Aluminosilicate Glasses," *J. Am. Ceram. Soc.*, vol. 73, no. 10, pp. 2848–2856, 1990, doi: 10.1111/j.1151-2916.1990.tb06685.x.

[68] Y. Shaharyar *et al.*, "Elucidating the Effect of Iron Speciation (Fe2+/Fe3+) on Crystallization Kinetics of Sodium Aluminosilicate Glasses," *J. Am. Ceram. Soc.*, vol. 99, no. 7, pp. 2306–2315, 2016, doi: 10.1111/jace.14239.

[69] M. Ren, X. Lu, L. Deng, P. H. Kuo, and J. Du, "B2O3/SiO2 substitution effect on structure and properties of Na2O-CaO-SrO-P2O5-SiO2 bioactive glasses from molecular dynamics simulations," *Phys. Chem. Chem. Phys.*, vol. 20, no. 20, pp. 14090–14104, 2018, doi: 10.1039/c7cp08358k.

[70] K. D. Jayasuriya, H. S. C. O'Neill, A. J. Berry, and S. J. Campbell, "A Mössbauer study of the oxidation state of Fe in silicate melts," *Am. Mineral.*, vol. 89, no. 11–12, pp. 1597–1609, Nov. 2004, doi: 10.2138/am-2004-11-1203.

[71] C. T. Prewitt and C. W. Burnham, "The crystal structure of jadeite, NaAlSi2O6," *Am. Mineral.*, vol. 51, no. 7, pp. 956–975, Jul. 1966.

[72] B. Ravel and M. Newville, "ATHENA and ARTEMIS Interactive Graphical Data

Analysisusing IFEFFIT," *Phys. Scr.*, p. 1007, 2005, doi: 10.1238/Physica.Topical.115a01007.

[73] W. Loewenstein, "The distribution of aluminum in the tetrahedra of silicates and aluminates," *Am. Mineral.*, vol. 39, no. 1–2, pp. 92–96, 1954.

[74] M. I. Tuheen and J. Du, "Effect of modifier cation field strength on the structures of magnesium oxide containing aluminoborosilicate glasses," *Int. J. Appl. Glas. Sci.*, Jul. 2022, doi: 10.1111/ijag.16599.